

Implicit Neural Representation for Video and Image Super-Resolution

Mary Aiyetigbo*, Wanqi Yuan*, Feng Luo, Nianyi Li,
Clemson University

{maiyeti, wanqiy, luofeng, nianyil}@clemson.edu

Abstract

We present a novel approach for super-resolution that utilizes implicit neural representation (INR) to effectively reconstruct and enhance low-resolution videos and images. By leveraging the capacity of neural networks to implicitly encode spatial and temporal features, our method facilitates high-resolution reconstruction using only low-resolution inputs and a 3D high-resolution grid. This results in an efficient solution for both image and video super-resolution. Our proposed method, SR-INR, maintains consistent details across frames and images, achieving impressive temporal stability without relying on the computationally intensive optical flow or motion estimation typically used in other video super-resolution techniques. The simplicity of our approach contrasts with the complexity of many existing methods, making it both effective and efficient. Experimental evaluations show that SR-INR delivers results on par with or superior to state-of-the-art super-resolution methods, while maintaining a more straightforward structure and reduced computational demands. These findings highlight the potential of implicit neural representations as a powerful tool for reconstructing high-quality, temporally consistent video and image signals from low-resolution data.

1. Introduction

High-resolution (HR) images and videos are essential for numerous computer vision applications, including surveillance, medical imaging, and multimedia entertainment. However, capturing high-resolution data is often constrained by hardware limitations, bandwidth, and storage considerations. Consequently, super-resolution (SR) techniques, which aim to reconstruct HR content from low-resolution (LR) inputs, have become a critical area of research [43]. Existing SR methods can be broadly categorized into single-image super-resolution (SISR) and video super-resolution (VSR). SISR methods focus on enhancing individual frames without leveraging temporal informa-

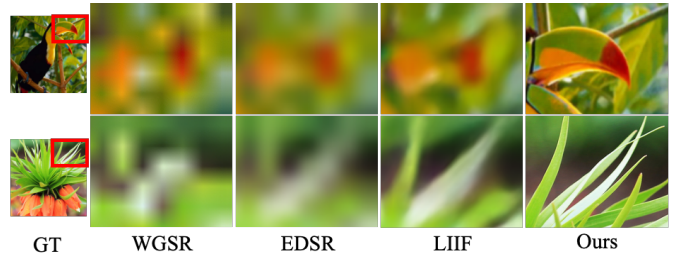


Figure 1. Visual comparison of image details in SOTA super-resolution. The leftmost column shows the ground truth, followed from left to right by the results of WGSR [26], EDSR [36], LIIF [12], and our method, with an upsampling scale of 32.

tion [27, 32, 66]. While these approaches have achieved impressive results, they often fail to produce temporally consistent outputs when applied to video sequences due to the lack of temporal modeling [7].

VSR methods exploit temporal correlations between consecutive frames to improve reconstruction quality and ensure temporal consistency [8, 23, 51, 54]. VSR approaches account for motion either by computing explicit motion estimation, using optical flow, to align frames before reconstruction [7, 23]. or implicitly motion through convolutions, dynamic filters, or transformer networks to capture long-range dependencies in both spatial and temporal dimensions, enhancing temporal consistency and reconstruction quality [14, 22, 33, 34, 39, 45, 52, 54, 57, 59, 67].

Implicit Neural Representations (INRs)[3, 40, 47, 50] have emerged as a powerful paradigm for continuous image and video representation. By representing signals as continuous functions parameterized by neural networks, INRs enable reconstruction at arbitrary resolutions without relying on discrete grids. This property makes them particularly suitable for super-resolution tasks, where flexible upsampling capabilities and the ability to model high-frequency details are essential. Recent advancements have extended Implicit Neural Representations (INRs) to super-resolution tasks for images and videos [12, 29]. LIIF [12] enables continuous upsampling using local implicit functions, while Bhat *et al.* [6] enhances modeling of com-

¹Equal contribution.

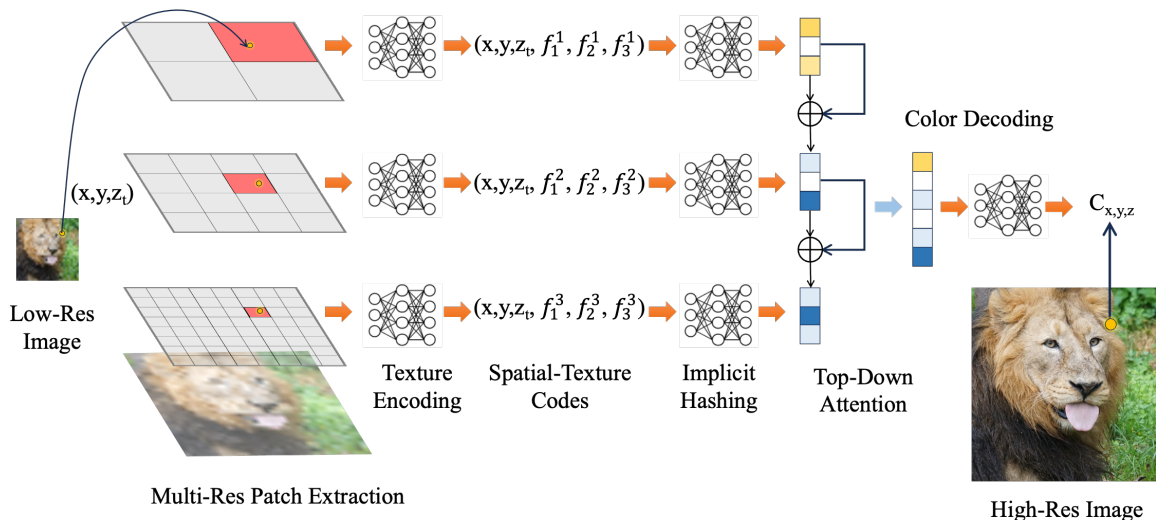


Figure 2. SR-INR pipeline for super-resolution. Local patches are extracted at multiple resolutions and processed by MLPs to generate feature vectors. These vectors are concatenated, refined via a top-down attention mechanism, and fed into an MLP to predict the RGB value, resulting in the super-resolved output.

plex structures with deep implicit functions. NeRV [13] and HNeRV [18] model videos by mapping temporal indices to high-resolution frames, implicitly capturing temporal correlations. VideoINR [11] represents videos as continuous space-time functions, allowing both spatial and temporal super-resolution at arbitrary resolutions and frame rates. However, existing INR-based methods are typically designed specifically for either images [6, 12] or videos [11, 13], limiting their flexibility when both modalities need to be addressed within a unified framework. In contrast, our approach is capable of handling both image and video super-resolution tasks. Inspired by Instant Neural Graphics Primitives (Instant-NGP) [41], which efficiently represent scenes using multi-resolution hash encoding, we extend this concept to super-resolution tasks.

In this paper, we propose a novel approach to super-resolution that leverages Implicit Neural Representations (INRs) and multi-resolution hash encoding for efficient high-resolution reconstruction from low-resolution videos and images. Our method, SR-INR, utilizes grid-based encoders with hierarchical representation learning to capture spatial and temporal features effectively. By implicitly encoding the input data and corresponding coordinates, our approach enables high-resolution reconstruction.

Our main contributions are as follows:

- We propose hierarchical grid-based encoding that leverages multi-resolution hash encoding in [41] to construct Implicit Neural Representations (INRs) for super-resolution tasks.
- Unlike prior methods that are tailored specifically for either images or videos, our framework is unified and capable of handling both image and video super-resolution.

- We provide extensive experiments and analyses to validate the effectiveness of our method. We demonstrate that our approach achieves competitive or superior results compared to state-of-the-art super-resolution methods.

2. Related Work

2.1. Image Super Resolution (ISR)

The introduction of deep learning for ISR began with SRCNN by Dong *et al.* [16], marking a significant milestone in super-resolution. Following this, numerous deep learning-based approaches were developed to enhance performance. Kim *et al.* [25] proposed the Very Deep Super-Resolution (VDSR) network, which utilized deeper architectures and residual learning to improve performance. Residual connections became essential in SR networks to address training difficulties in deep models. Ledig *et al.* [28] employed generative adversarial networks (GANs) with a residual network (RESNET) [20] backbone to produce more realistic textures. Lim *et al.* [36] proposed the Enhanced Deep Residual Network (EDSR), improving efficiency by removing unnecessary layers such as batch normalization. Zhang *et al.* introduced the Residual Channel Attention Network (RCAN) [65], incorporating channel attention mechanisms to adaptively rescale features. The success of vision transformers [17] and their ability to model long-range dependencies led to the use of attention mechanisms in ISR. Dai *et al.* proposed the Second-order Attention Network (SAN) [15], which captured feature interdependencies using second-order statistics. Liang *et al.* introduced SwinIR [32], utilizing Swin Transformers [38] with hierarchical feature maps and shifted windows to capture both local and

global information effectively. Generative models, such as GANs and diffusion models, have also been highly effective for super-resolution tasks [55, 63].

2.2. Video Super Resolution (VSR)

Video super-resolution (VSR) leverages temporal information from adjacent frames, presenting challenges like motion estimation and alignment. VSR methods can be broadly classified into sliding window and recurrent methods. Sliding window methods process consecutive frames together to reconstruct a high-resolution frame. [7, 23, 31] relied on explicit motion estimation to align neighboring frames, which made them heavily dependent on accurate optical flow, prone to errors in complex scenes. To overcome this dependency, other approaches [22, 51, 58, 60] adopted implicit motion estimation. Deformable convolutions [52, 54, 56] proved effective in capturing spatial and temporal dependencies without explicit motion estimation. The Video Restoration Transformer (VRT) [35] further enhanced performance by capturing long-range dependencies. Recurrent methods [8, 9, 19, 21, 34, 44–46, 61] excel at capturing long-term temporal information by processing frames sequentially while maintaining a hidden state. These methods effectively handle complex motion and model temporal dependencies.

2.3. Implicit Neural Representation for Super-Resolution

Implicit Neural Representations (INRs) have emerged as an effective approach for modeling continuous image and video data by representing signals as continuous functions parameterized by neural networks. This allows high-quality reconstruction and super-resolution at arbitrary scales. Chen *et al.* introduced the Local Implicit Image Function (LIIF) [12], which learns continuous representations using local implicit functions, enabling upsampling to arbitrary resolutions. Bhat *et al.* proposed Deep Implicit Functions [6] to handle complex image structures, while SIREN [47] demonstrates that periodic activation functions help represent complex natural signals for super-resolution tasks. Tancik *et al.* presented Fourier Features [50] to enable networks capture fine details.

Soh *et al.* introduced PIIFGAN [48], leveraging periodic implicit functions for general image super-resolution across various scaling factors. An *et al.* proposed HyperINR [2], using a hypernetwork to generate the weights of an INR conditioned on image content. For video super-resolution, Chen *et al.* proposed NeRV [13], which models videos by mapping frame indices to high-resolution frames without explicit pixel storage. Han *et al.* extended this with HNeRV [18], combining implicit and explicit representations. Chen *et al.* also introduced VideoINR [11], modeling videos as continuous functions over space and time, allowing for

both spatial and temporal super-resolution at arbitrary resolutions and frame rates. Lee *et al.* combined INRs with learned encoders for image super-resolution [30], while Batzolis *et al.* proposed Implicit Diffusion Models [4], combining INRs with diffusion processes to generate high-resolution images from low-resolution inputs.

Our method draws inspiration from Instant-NGP [41], utilizing multi-resolution hash encoding for efficient neural representation. While Instant-NGP focuses on 3D scene reconstruction, we adapt its multi-resolution hash embedding approach to the super-resolution domain for both images and videos. This allows us to achieve efficient and high-quality super-resolution, generalizing across diverse 2D image and video data. Other works, such as DirectVoxGO [49], TensoRF [10], and Plenoxels [62], utilize similar encoding techniques for 3D scene representation and rendering. However, these methods are designed for 3D tasks and do not address image and video super-resolution. Our work differs by applying these encoding strategies to super-resolution tasks, demonstrating the versatility of grid-based and hash embedding techniques beyond 3D applications.

3. Method

In this section, we describe our proposed method, SR-INR, for image and video super-resolution. We start by defining the problem, then provide detailed explanations of each stage in our pipeline: texture encoding, implicit hashing, and top-down attention.

3.1. Problem Definition

The input to SR-INR is a batch of low-resolution frames $I_{lr} \in \mathbb{R}^{H_{lr} \times W_{lr} \times C}$, and a high-resolution grid \mathcal{G}_{hr} specifying the locations of the high-resolution pixel coordinates. The output is the RGB color value corresponding to each high-resolution coordinate. Mathematically, we denote this as:

$$I_{hr} = f(I_{lr}, \mathcal{G}_{hr}), \quad (1)$$

where $I_{hr} \in \mathbb{R}^{H_{hr} \times W_{hr} \times C}$ represents the reconstructed high-resolution image.

3.2. Texture Encoding

The texture encoding process starts by extracting local patches from the low-resolution images based on a batch of resolution grids. Inspired by Instant-NGP [41], we adopt a strategy of using a multi-resolution grid to generate local feature representations. Specifically, given a high-resolution pixel coordinate, we extract multi-scale local patches from the low-resolution frames based on the resolution grid:

$$P_i^r = g(I_{lr}, \mathcal{G}_r), \quad (2)$$

where P_i^r represents a local patch centered around coordinate i at resolution level r . The size of the local patch is

determined by the resolution grid \mathcal{G}_r .

We then predict a fixed-length feature code for each of these multi-resolution patches:

$$\hat{\mathcal{F}}_i^r = f_\theta^r(P_i^r), \quad (3)$$

where $\mathcal{F}_i^r \in \mathbb{R}^3$ is a continuous feature code, ranging $[-1, 1]$, indicating the location of the local texture in the hidden feature space. In our implementation, we use a three-dimensional feature code to represent the local texture information.

For each pixel in the high-resolution grid, we concatenate the feature codes from multiple resolutions to obtain a six-dimensional representation:

$$\mathcal{F}_i^r = [x, y, z_t, \hat{\mathcal{F}}], \quad (4)$$

where $[x, y, z_t]$ represents the pixel coordinate in 3D space, and \mathcal{F}_i^r represents the local texture features from multiple resolutions.

3.3. Implicit Hashing

To obtain the implicit feature vectors for a given coordinate in the 6D latent space, we leverage a spatial hash table. The hash table stores trainable feature vectors in a compact manner, allowing us to efficiently retrieve feature codes for neighboring coordinates.

For a given high-resolution coordinate, we find the neighboring locations in the latent space and use the hash table to retrieve their feature vectors:

$$\{\mathcal{F}_{N_D}^r\} = \text{HashTable}(\mathcal{F}_i), \quad (5)$$

where $\{\mathcal{F}_{N_D}^r\}$ represents the feature vectors of the neighboring nodes in the latent space.

We then use a network to predict weights for combining the neighboring features. As we encode the local features using a 6D code (where the first three dimensions indicate the spatial location of the coordinates, and the last three dimensions, predicted by f_θ^r , indicate the coordinates of local texture in the implicit texture codebook, which is unknown), the number of neighbors in the 6D space will be 2^D (where $D = 6$ in our implementation). Directly interpolating feature vectors in this high-dimensional space is computationally intensive, and the unknown nature of the feature codebook adds further complexity. To address this, we use a network to predict the weights for each neighbor:

$$\text{weight}_N^r = f_H(\mathcal{F}_i^r, \mathcal{F}_i^r - \mathcal{F}_i^r(\min), \mathcal{F}_i^r(\max) - \mathcal{F}_i^r), \quad (6)$$

where $\mathcal{F}_i^r(\min)$ and $\mathcal{F}_i^r(\max)$ represent the bottom and top boundaries of the high-dimensional vertex, respectively. The final feature vector at resolution layer r is obtained by a weighted sum of the neighboring feature vectors:

$$\mathcal{F}_p^r = \sum \text{weight}_N^r \cdot \mathcal{F}_{N_D}^r. \quad (7)$$

3.4. Top-Down Attention for Feature Concatenation

To generate the final feature vector, we apply a top-down attention mechanism to integrate features from different resolution layers. We start from the top layer and iteratively update the feature vectors using attention weights:

$$\text{att}_w^{r+1} = f_{\text{att}}(\mathcal{F}_p^r), \quad (8)$$

$$\mathcal{F}_p^{r+1} = \text{att}_w^{r+1} \cdot \mathcal{F}_p^{r+1}. \quad (9)$$

After applying the attention weights, we concatenate the updated feature vectors from all resolution layers to form the final feature representation:

$$\mathcal{F}_p = [\mathcal{F}_p^1, \mathcal{F}_p^2, \dots, \mathcal{F}_p^R]. \quad (10)$$

The final RGB color value for each high-resolution pixel is then predicted using a two-layer MLP:

$$C_p = f_C(\mathcal{F}_p), \quad (11)$$

where f_C is the MLP used to map the concatenated feature vector to the RGB color value.

All networks used in our pipeline are two-layer MLPs with one hidden layer of 64 nodes.

3.5. Training Details.

Due to the pixel-based encoding and decoding nature of our method, using a simple mean squared error (MSE) loss often introduces artifacts. These artifacts occur because MSE loss equally penalizes all pixels, causing the network to overlook subtle yet critical details in regions with small reconstruction errors, which can lead to over-smoothing. To address this issue, we introduce a novel Pixel-Error Amplified Loss (PEA-loss).

Specifically, the PEA-loss is designed to amplify reconstruction errors for low-error regions to encourage the model to refine these areas further. The loss is defined as follows:

First, we calculate the per-pixel reconstruction error:

$$\mathcal{L}_{\text{pixel}} = \text{MSE}(C_p, C_{\text{gt}}), \quad (12)$$

where C_p is the predicted RGB value, and C_{gt} is the ground truth RGB value. Next, we apply a reconstruction mask to emphasize areas with higher errors. Initially, the reconstruction mask is set to all ones, we then update the reconstruction mask by masking out pixels with low reconstruction error:

$$M_{\text{recon}} = \begin{cases} M_{\text{recon}}, & \text{if } \mathcal{L}_{\text{pixel}} > \tau, \\ 0, & \text{otherwise,} \end{cases} \quad (13)$$

where τ is a predefined threshold for masking low-error pixels. The masked loss is then calculated as:

$$\mathcal{L}_{\text{masked}} = \text{mean}(\mathcal{L}_{\text{pixel}} \cdot M_{\text{recon}}), \quad (14)$$

Additionally, we introduce a boosted loss for regions with small errors to further refine details:

$$\mathcal{L}_{\text{boost}} = f_{\text{boost}}(C_p, C_{\text{gt}}) = \mathcal{L}_{\text{pixel}} + M_{\text{boost}} \cdot \delta, \quad (15)$$

with M_{boost} defined as:

$$M_{\text{boost}} = \begin{cases} 1, & \text{if } \mathcal{L}_{\text{pixel}} < \epsilon, \\ 0, & \text{otherwise,} \end{cases} \quad (16)$$

where ϵ is a small threshold for boosting low-error pixels, and δ is a small constant added to amplify the loss.

The final PEA-loss is given by:

$$\mathcal{L}_{\text{PEA}} = \mathcal{L}_{\text{recon}} + \alpha \cdot \mathcal{L}_{\text{boost}} \quad (17)$$

where α is the parameter to control the boosting impact. A detailed analysis of the loss related parameters can be found in our Supplementary material.

4. Experiments

4.1. Image Super Resolution

For our image super-resolution experiments, we evaluated the proposed method on several benchmark datasets, including DIV2K [1] from the NTIRE 2017 Challenge [53], CelebA-HQ [24], Set5 [5], and Set14 [64]. We trained our model separately on each dataset to assess its performance across different image domains and characteristics. For DIV2K, we center-cropped each image to 1024×1024 pixels and downsampled them to 512×512 pixels using bicubic interpolation; this 512×512 resolution served as the HR ground truth for our experiments. For CelebA-HQ, we downsampled the images directly to 512×512 pixels to obtain the HR images. The Set5 and Set14 datasets were used as provided and adjusted to match our target low-resolution (LR). We generated the LR inputs with scaling factors of $\times 2$, $\times 4$, $\times 8$, $\times 16$, and $\times 32$.

To validate the effectiveness of the proposed method, we conducted comprehensive experimental evaluations on several widely used benchmark datasets and compared its performance with state-of-the-art approaches (WGSR [26], EDSR [36], LIIF [12]). The experimental results demonstrate that our method achieved strong performance in reconstructing high-quality HR images from LR inputs, even at large scaling factors. The results indicated that our model effectively handles high-scale super-resolution, preserving fine details and textures across different datasets.

4.2. Quantitative Analysis

Table 1 presents the quantitative evaluation results on four benchmark datasets. On the DIV2K dataset, our method achieves a PSNR of 27.130 at $\times 32$ scale, representing a

39.5% improvement over LIIF, 57.1% and 68.8% improvements over EDSR and WGSR, respectively. This performance advantage is consistent across all super-resolution scales, particularly in challenging high-scale scenarios. On the CelebA-HQ dataset, at $\times 32$ scale, our method achieves 43.8% and 6.9% improvements on PSNR and SSIM respectively, over the best-performing LIIF method. Notably, on the Set14 dataset, the PSNR of our method increased from 30.030 at $\times 4$ to 37.040 at $\times 32$. This counterintuitive result suggests that our approach is better equipped to capture and reconstruct the intrinsic features of images at extremely high super-resolution scale.

4.3. Qualitative Analysis

Figure 4 showcases a visual comparison of results under $\times 32$ scale. In the face reconstruction tests on the CelebA-HQ dataset, existing methods commonly exhibit significant detail loss. Images generated by WGSR and EDSR display noticeable blurring and structural distortions. While LIIF shows some improvement in preserving overall facial structures, it struggles to capture critical details in areas such as the eyes and facial contours. In contrast, our method not only accurately maintains the overall facial structure but also successfully restores fine features like eyes and hair strands, achieving a visual quality highly consistent with the ground truth. For handling complex textures, the wolf fur images from DIV2K and butterfly wings from Set5 serve as representative cases. Traditional methods often result in over-smoothing or structural deformation when processing such high-frequency details, leading to a loss of texture information. Our method effectively overcomes these limitations, accurately reconstructing the intricate textures of wolf fur and precisely restoring the complex patterns and structures of butterfly wings. Notably, for the primate facial images in the Set14 dataset, our method demonstrates exceptional color fidelity when handling abrupt transitions between red and blue hues, avoiding common issues of color distortion and edge blurring seen in other approaches. Figure 3 shows the generalizable ability of our method. We trained our model at a scale of $\times 32$ and subsequently applied it to super-resolution tasks at scales of $\times 2$, $\times 4$, $\times 8$, $\times 16$, $\times 64$, and $\times 128$, demonstrating the excellent generalization performance of our method across all scales overall.

4.4. Video Super Resolution

To showcase the effectiveness of our model in video super-resolution, we conducted experiments on the Vid4 [37] and GOPRO [42] video datasets. These datasets contain diverse content and motion patterns, providing a comprehensive evaluation of our method’s capability to handle temporal information. For the experiments, we processed the video frames by resizing the HR video frames to 256×256 pixels to serve as the ground truth. The low-resolution video

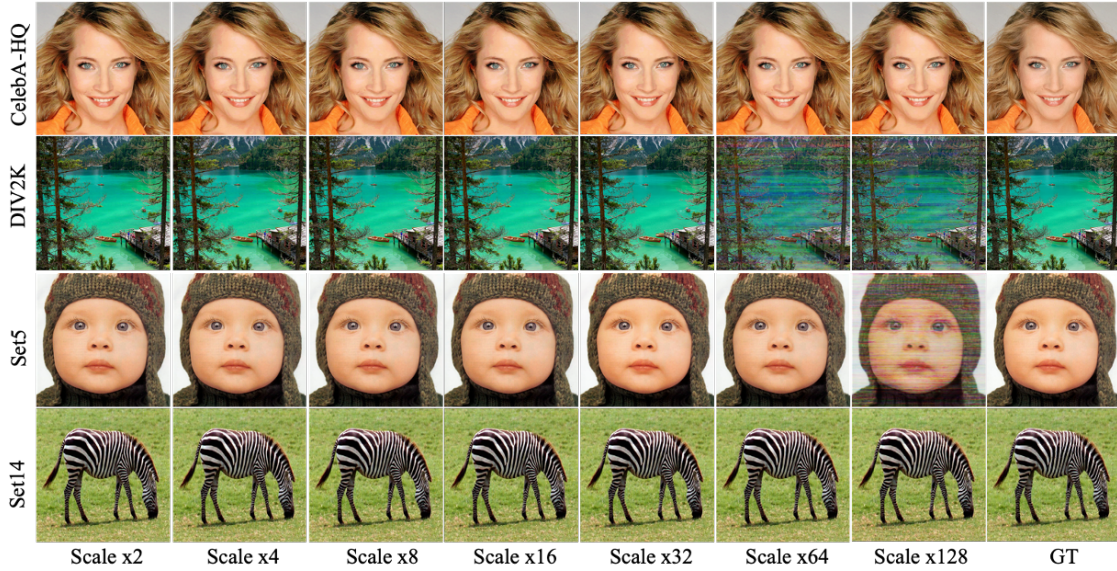


Figure 3. Generalization capability of our method. Trained with an upsampling scale of $\times 32$, our method is subsequently applied to super-resolution tasks at scales of $\times 2$, $\times 4$, $\times 8$, $\times 16$, $\times 64$, and $\times 128$.

Datasets	Methods	Scale x4		Scale x8		Scale x16		Scale x32	
		PSNR	SSIM	PSNR	SSIM	PSNR	SSIM	PSNR	SSIM
DIV2K	LIIF	27.364	0.849	24.012	0.760	21.462	0.675	19.444	0.607
	EDSR	25.739	0.753	21.076	0.511	19.001	0.430	17.273	0.395
	WGSR	29.188	0.820	20.187	0.517	17.957	0.438	16.074	0.400
	Ours	27.870	0.807	25.930	0.846	26.230	0.859	27.130	0.892
CelebA-HQ	LIIF	33.285	0.949	30.442	0.928	27.433	0.913	24.256	0.887
	EDSR	31.879	0.843	27.233	0.726	24.144	0.665	21.186	0.618
	WGSR	22.669	0.519	26.336	0.726	23.181	0.668	20.110	0.620
	Ours	34.205	0.923	34.250	0.927	34.430	0.932	34.875	0.948
Set5	LIIF	32.294	0.963	26.982	0.921	23.013	0.873	20.329	0.806
	EDSR	33.984	0.911	25.744	0.729	22.098	0.630	19.090	0.574
	WGSR	31.508	0.869	25.469	0.758	21.378	0.657	18.159	0.592
	Ours	22.180	0.614	22.770	0.628	23.390	0.671	35.610	0.982
Set14	LIIF	28.671	0.920	24.938	0.822	22.134	0.745	19.824	0.708
	EDSR	27.879	0.792	22.152	0.557	19.737	0.474	17.882	0.442
	WGSR	26.689	0.716	21.568	0.585	18.749	0.499	16.821	0.462
	Ours	30.030	0.791	31.780	0.849	32.410	0.851	37.040	0.961

Table 1. Quantitative comparison on image datasets including DIV2K, CelebA-HQ, Set5 and Set14. The best result is highlighted in bold.

Method	Vid4		GOPRO	
	PSNR	SSIM	PSNR	SSIM
VRT	23.780	0.672	28.800	0.854
VideoINR	25.610	0.771	29.410	0.867
Ours	30.760	0.945	27.612	0.856

Table 2. Quantitative comparison on video datasets including Vid4 and GOPRO. Best result in PSNR and SSIM is highlighted in bold.

Method	Vid4		GOPRO	
	PSNR	SSIM	PSNR	SSIM
NERV	35.446	0.976	32.028	0.970
Ours	30.760	0.945	27.612	0.856

Table 3. Quantitative comparison on video datasets including Vid4 and GOPRO. The best result in PSNR and SSIM is highlighted in bold.

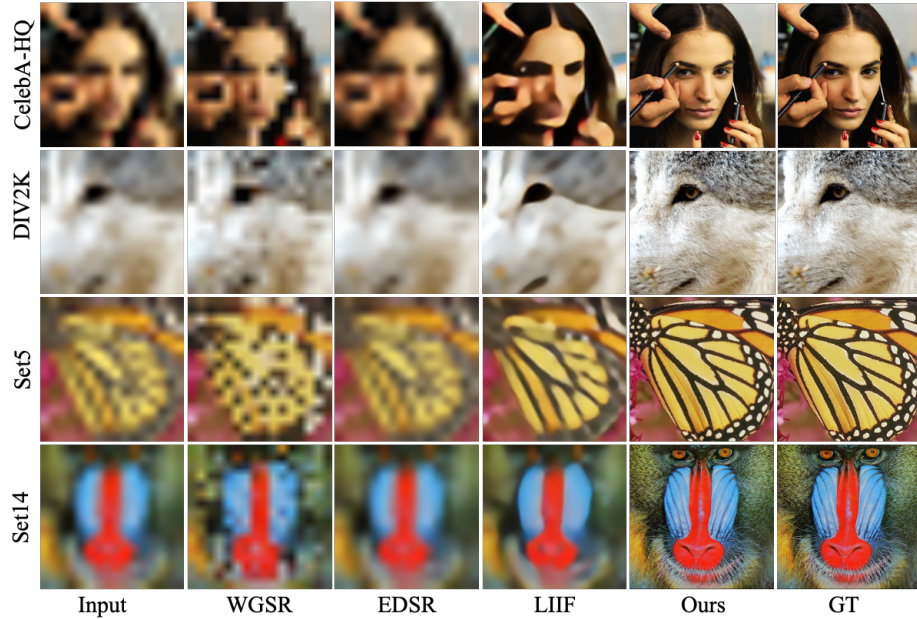


Figure 4. Visual comparison of SOTA in Image SR. From top to bottom, the datasets displayed are CelebA-HQ, DIV2K, Set5, and Set14. The leftmost column shows the input images, while the rightmost column displays the ground truth. The upsampling scale is set to $\times 32$.

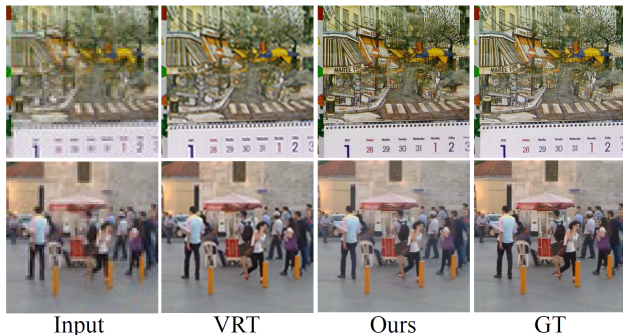


Figure 5. This image shows the results of VRT and Ours. From top to bottom, the datasets displayed are Vid4 and GOPRO datasets.

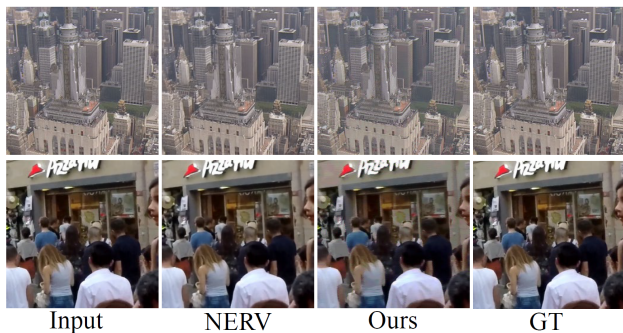


Figure 6. This image shows results of NERV and Ours. From top to bottom, the datasets displayed are Vid4 and GOPRO datasets.

sequences were generated by downsampling the HR frames using a scaling factor of $\times 4$ with bicubic interpolation, re-

sulting in LR frames of 64×64 pixels. Our model was trained to reconstruct the HR frames from the LR inputs, effectively learning to capture both spatial details and temporal consistency across frames.

We evaluated the performance of our model on video super-resolution tasks by comparing it with state-of-the-art methods, specifically the Video Restoration Transformer (VRT)[33] and VideoINR[11]. Our experiments were conducted using a scaling factor of $\times 4$, where the low-resolution input frames are 64×64 pixels, and the high-resolution outputs are 256×256 pixels. As shown in Figure 5, our model is capable of generating high-quality results. The quantitative results presented in Table 2 indicate that our model achieves the best performance on the VID4 dataset and comparable results on the GOPRO dataset. Additionally, we compared our method with the video generation model NeRV [13], which is trained on high-resolution videos. Despite the differences in training conditions, our model is able to produce high-quality video outputs, as demonstrated in Figure 6. The comparative results in Table 3 further confirm the effectiveness of our approach in generating good quality videos.

4.5. Implementaion Details.

All the networks used are two-layer Multi-Layer Perceptrons (MLPs) with ReLU activation functions and hidden layer dimensions of 64 units. The training utilized the Mean Squared Error (MSE) loss function to optimize the model parameters. For evaluation, we considered scaling factors of

$n_{base_resolution}$	PSNR	SSIM	Memory	Parameters
$n = 2$	45.576	0.991	3.06G	4.074×10^8
$n = 4$	42.372	0.981	3.03G	4.038×10^8
$n = 8$	45.080	0.988	3.02G	4.030×10^8
$n = 16$	44.422	0.980	3.02G	4.028×10^8
$n = 32$	43.272	0.976	3.02G	4.027×10^8

Table 4. Ablation study on the initial grid resolution of the first level. The best result in PSNR and SSIM is highlighted in bold.

$n_{features_per_level}$	PSNR	SSIM	Memory	Parameters
$n = 2$	41.847	0.981	3.03G	4.039×10^8
$n = 4$	48.174	0.992	6.03G	8.066×10^8

Table 5. Ablation study on the number of feature codes per level in the hash table. The best result in PSNR and SSIM in bold.

$\times 2$, $\times 4$, $\times 8$, $\times 16$, and $\times 32$, generating the low-resolution images using bicubic downsampling to simulate different levels of image degradation. Our model was trained specifically on the $\times 32$ scaling factor for 300 epochs on each dataset, employing a batch size of 32. We used the Adam optimizer with an initial learning rate of 1×10^{-4} . Learning rate was reduced by a factor of 0.5 every 100 epochs. All experiments were conducted on an NVIDIA A100 GPU.

4.6. Ablation Studies

We conduct extensive ablation studies to investigate the impact of various architectural choices and hyperparameters on our model’s performance on a subset of CelebA-HQ with 100 images and resolution of 128×128 . We evaluate the model using PSNR and SSIM metrics while also considering memory consumption and parameter count. All experiments maintain consistent settings except for the specifically varied component.

Initial Grid Resolution. As shown in Table 4, we experiment with different resolutions ranging from $n = 2$ to $n = 32$. The results demonstrate that a smaller initial grid resolution ($n = 2$) achieves the best performance with PSNR = 45.576 and SSIM = 0.991, while maintaining comparable memory usage to other configurations. This suggests that starting with a finer grid resolution allows the model to capture more detailed features from the beginning of the network.

Feature Codes per Level. Table 5 presents the impact of varying the number of feature codes per level in the hash table. Increasing the feature codes from $n = 2$ to $n = 4$ leads to a substantial improvement in performance on PSNR for 15.0% and on SSIM for 1.1%. However, this enhancement comes at the cost of doubled memory consumption and parameter count. This trade-off suggests that additional feature codes enable better representation capacity but require more computational resources.

Hash Table Size. The size of the hash table per level proves

$n_{log2_hashmap_size}$	PSNR	SSIM	Memory	Parameters
$n = 10$	13.813	0.245	0.03G	1.259×10^6
$n = 20$	36.333	0.964	0.22G	2.640×10^7
$n = 22$	39.858	0.977	0.78G	1.019×10^8
$n = 24$	42.871	0.984	3.03G	4.039×10^8
$n = 26$	44.533	0.988	6.03G	1.612×10^9

Table 6. Ablation study on the size of the hash table per level. The best result in PSNR and SSIM is highlighted in bold.

n_{levels}	PSNR	SSIM	Memory	Parameters
$n = 2$	30.517	0.877	0.52G	6.715×10^7
$n = 4$	34.835	0.924	1.02G	1.347×10^8
$n = 6$	36.662	0.949	1.52G	2.018×10^8
$n = 8$	41.581	0.981	2.03G	2.693×10^8
$n = 10$	44.239	0.981	2.53G	3.364×10^8
$n = 12$	41.117	0.976	3.03G	4.039×10^8
$n = 14$	42.344	0.988	3.53G	4.710×10^8
$n = 16$	43.155	0.987	4.03G	5.385×10^8

Table 7. Ablation study on the number of res-layers. The best result in PSNR and SSIM is highlighted in bold.

$n_{finest_resolution}$	PSNR	SSIM	Memory	Parameters
$n = 64$	31.794	0.939	6.02G	4.030×10^8
$n = 128$	39.990	0.976	6.04G	4.039×10^8

Table 8. Ablation study on the number of the final grid resolution of the bottom level. The best result in PSNR and SSIM is highlighted in bold.

to be a crucial factor in model performance, as evidenced in Table 6. We examine different hash table sizes by varying from 10 to 26. A clear trend emerges where larger hash tables consistently yield better results, the best performance achieved at $n = 26$ with PSNR = 44.533 and SSIM = 0.988. However, this improvement comes with a significant increase in memory usage and parameter count, growing from 0.03G to 6.03G. Notably, there appears to be a sweet spot around $n = 24$, where we achieve good performance (PSNR=42.871) with more moderate resource requirements.

Number of Res-layers. Table 7 investigates the impact of varying the number of res-layers from 2 to 16. The results show that performance generally improves with more layers up to a point, with optimal PSNR achieved at $n = 10$ layers and best SSIM at $n = 14$ layers. Notably, adding more layers beyond $n = 10$ doesn’t consistently improve performance, suggesting that the model reaches a point of diminishing returns. The memory usage scales linearly with the number of layers, increasing from 0.52G to 4.03G.

Final Grid Resolution. The final grid resolution of the bottom level, examined in Table 8, shows that increasing the resolution from 64 to 128 significantly improves performance on PSNR with 25.7% and SSIM with 3.9%. This im-

provement comes with only a marginal increase in memory usage, suggesting that a higher final resolution is beneficial for capturing fine details in the output.

These findings provide valuable guidance for configuring the model architecture to achieve the desired balance between performance and computational efficiency.

References

- [1] Eirikur Agustsson and Radu Timofte. NTIRE 2017 challenge on single image super-resolution: Dataset and study. In *2017 IEEE Conference on Computer Vision and Pattern Recognition Workshops, CVPR Workshops 2017, Honolulu, HI, USA, July 21-26, 2017*, pages 1122–1131. IEEE Computer Society, 2017. 5
- [2] Shiqi An, Gwangjin Lee, Tae Hyun Oh, and Kyoung Mu Kim. Hyperinr: Learning hyper network for continuous image representation with applications to super-resolution. In *Advances in Neural Information Processing Systems*, pages 17421–17432, 2021. 3
- [3] Jonathan T Barron, Ben Mildenhall, Matthew Tancik, Peter Hedman, Ricardo Martin-Brualla, and Pratul P Srinivasan. Mip-nerf: A multiscale representation for anti-aliasing neural radiance fields. In *Proceedings of the IEEE International Conference on Computer Vision*, pages 5855–5864, 2021. 1
- [4] Evangelos Batzolis, Silvia L. Pinteá, Maurice-Jan Kraak, and Jan C. van Gemert. Implicit diffusion models for continuous super-resolution. *arXiv preprint arXiv:2207.12527*, 2022. 3
- [5] Marco Bevilacqua, Aline Roumy, Christine Guillemot, and Marie-Line Alberi-Morel. Low-complexity single-image super-resolution based on nonnegative neighbor embedding. In *British Machine Vision Conference, BMVC 2012, Surrey, UK, September 3-7, 2012*, pages 1–10. BMVA Press, 2012. 5
- [6] Shahrukh Athar Bhat, Bernhard Kainz, and Michael O’Boyle. Deep implicit functions for image reconstruction. In *Proceedings of the IEEE/CVF Conference on Computer Vision and Pattern Recognition*, pages 5649–5658, 2021. 1, 2, 3
- [7] Jose Caballero, Christian Ledig, Andrew Aitken, Alejandro Acosta, Johannes Totz, Zehan Wang, and Wenzhe Shi. Real-time video super-resolution with spatio-temporal networks and motion compensation. In *Proceedings of the IEEE conference on computer vision and pattern recognition*, pages 4778–4787, 2017. 1, 3
- [8] Kelvin CK Chan, Xintao Wang, Ke Yu, Chao Dong, and Chen Change Loy. Basicvsr: The search for essential components in video super-resolution and beyond. In *Proceedings of the IEEE/CVF conference on computer vision and pattern recognition*, pages 4947–4956, 2021. 1, 3
- [9] Kelvin CK Chan, Shangchen Zhou, Xiangyu Xu, and Chen Change Loy. Basicvsr++: Improving video super-resolution with enhanced propagation and alignment. In *Proceedings of the IEEE/CVF conference on computer vision and pattern recognition*, pages 5972–5981, 2022. 3
- [10] Anpei Chen, Zexiang Xu, Andreas Geiger, Jingyi Yu, and Hao Su. Tensorf: Tensorial radiance fields. In *Proceedings of the European Conference on Computer Vision*, pages 1–16, 2022. 3
- [11] Tao Chen, Jianmin Li, Xuanchong Jin, Haoqiang Fan, Nenghai Yu, and Jian Sun. Videoinr: Learning video implicit neural representation for continuous space-time super-resolution. In *Proceedings of the IEEE/CVF Conference on Computer Vision and Pattern Recognition*, pages 16105–16114, 2022. 2, 3, 7
- [12] Yinbo Chen, Sifei Liu, and Xiaolong Wang. Learning continuous image representation with local implicit image function. In *Proceedings of the IEEE/CVF Conference on Computer Vision and Pattern Recognition*, pages 8628–8638, 2021. 1, 2, 3, 5
- [13] Zhengyu Chen, Hexiang Wu, and Yuan-Fang Wang. Nerv: Neural representations for videos. In *Advances in Neural Information Processing Systems*, 2021. 2, 3, 7
- [14] Zhikai Chen, Fuchen Long, Zhaofan Qiu, Ting Yao, Wengang Zhou, Jiebo Luo, and Tao Mei. Learning spatial adaptation and temporal coherence in diffusion models for video super-resolution. In *Proceedings of the IEEE/CVF Conference on Computer Vision and Pattern Recognition*, pages 9232–9241, 2024. 1
- [15] Tao Dai, Jianrui Cai, Yongbing Zhang, Shu-Tao Xia, and Lei Zhang. Second-order attention network for single image super-resolution. In *Proceedings of the IEEE/CVF conference on computer vision and pattern recognition*, pages 11065–11074, 2019. 2
- [16] Chao Dong, Chen Change Loy, Kaiming He, and Xiaoou Tang. Image super-resolution using deep convolutional networks. *IEEE transactions on pattern analysis and machine intelligence*, 38(2):295–307, 2015. 2
- [17] Alexey Dosovitskiy. An image is worth 16x16 words: Transformers for image recognition at scale. *arXiv preprint arXiv:2010.11929*, 2020. 2
- [18] Rui Han, Zhengyu Chen, and Yuan-Fang Wang. Hnerv: A hybrid neural representation for videos. In *Proceedings of the IEEE/CVF Conference on Computer Vision and Pattern Recognition*, pages 18966–18975, 2022. 2, 3
- [19] Muhammad Haris, Gregory Shakhnarovich, and Norimichi Ukita. Recurrent back-projection network for video super-resolution. In *Proceedings of the IEEE/CVF conference on computer vision and pattern recognition*, pages 3897–3906, 2019. 3
- [20] Kaiming He, Xiangyu Zhang, Shaoqing Ren, and Jian Sun. Deep residual learning for image recognition. In *Proceedings of the IEEE conference on computer vision and pattern recognition*, pages 770–778, 2016. 2
- [21] Yan Huang, Wei Wang, and Liang Wang. Video super-resolution via bidirectional recurrent convolutional networks. *IEEE transactions on pattern analysis and machine intelligence*, 40(4):1015–1028, 2017. 3
- [22] Younghyun Jo, Seoung Wug Oh, Jaeyeon Kang, and Seon Joo Kim. Deep video super-resolution network using dynamic upsampling filters without explicit motion compensation. In *Proceedings of the IEEE conference on computer vision and pattern recognition*, pages 3224–3232, 2018. 1, 3

- [23] Armin Kappeler, Seunghwan Yoo, Qiqin Dai, and Aggelos K Katsaggelos. Video super-resolution with convolutional neural networks. *IEEE transactions on computational imaging*, 2(2):109–122, 2016. 1, 3
- [24] Tero Karras, Timo Aila, Samuli Laine, and Jaakko Lehtinen. Progressive growing of gans for improved quality, stability, and variation. In *6th International Conference on Learning Representations, ICLR 2018, Vancouver, BC, Canada, April 30 - May 3, 2018, Conference Track Proceedings*. OpenReview.net, 2018. 5
- [25] Jiwon Kim, Jung Kwon Lee, and Kyoung Mu Lee. Accurate image super-resolution using very deep convolutional networks. In *Proceedings of the IEEE conference on computer vision and pattern recognition*, pages 1646–1654, 2016. 2
- [26] Cansu Korkmaz, A Murat Tekalp, and Zafer Dogan. Training generative image super-resolution models by wavelet-domain losses enables better control of artifacts. In *Proceedings of the IEEE/CVF Conference on Computer Vision and Pattern Recognition*, pages 5926–5936, 2024. 1, 5
- [27] Christian Ledig, Lucas Theis, Ferenc Huszár, Jose Caballero, Andrew Cunningham, Alejandro Acosta, Andrew Aitken, Alykhan Tejani, Johannes Totz, Zehan Wang, and Wenzhe Shi. Photo-realistic single image super-resolution using a generative adversarial network. In *Proceedings of the IEEE Conference on Computer Vision and Pattern Recognition*, pages 4681–4690, 2017. 1
- [28] Christian Ledig, Lucas Theis, Ferenc Huszár, Jose Caballero, Andrew Cunningham, Alejandro Acosta, Andrew Aitken, Alykhan Tejani, Johannes Totz, Zehan Wang, et al. Photo-realistic single image super-resolution using a generative adversarial network. In *Proceedings of the IEEE conference on computer vision and pattern recognition*, pages 4681–4690, 2017. 2
- [29] Doyup Lee, Chiheon Kim, Minsu Cho, and WOOK SHIN HAN. Locality-aware generalizable implicit neural representation. *Advances in Neural Information Processing Systems*, 36, 2024. 1
- [30] Jaeho Lee, Junyong Kim, Hyeongseok Kim, In-Young Jang, and Junsik Kim. Implicit neural representations with learned encoder for image super-resolution. *arXiv preprint arXiv:2203.01944*, 2022. 3
- [31] Wenbo Li, Xin Tao, Taian Guo, Lu Qi, Jiangbo Lu, and Jiaya Jia. Mucan: Multi-correspondence aggregation network for video super-resolution. In *Computer Vision—ECCV 2020: 16th European Conference, Glasgow, UK, August 23–28, 2020, Proceedings, Part X 16*, pages 335–351. Springer, 2020. 3
- [32] Jingyun Liang, Jiezhong Cao, Guolei Sun, Kai Zhang, Luc Van Gool, and Radu Timofte. Swinir: Image restoration using swin transformer. In *Proceedings of the IEEE/CVF international conference on computer vision*, pages 1833–1844, 2021. 1, 2
- [33] Jingyun Liang, Jiezhong Cao, Guolei Zhang, Luc Van Gool, and Radu Timofte. Vrt: A video restoration transformer. In *Advances in Neural Information Processing Systems*, 2022. 1, 7
- [34] Jingyun Liang, Yuchen Fan, Xiaoyu Xiang, Rakesh Ranjan, Eddy Ilg, Simon Green, Jiezhong Cao, Kai Zhang, Radu Timofte, and Luc V Gool. Recurrent video restoration transformer with guided deformable attention. *Advances in Neural Information Processing Systems*, 35:378–393, 2022. 1, 3
- [35] Jingyun Liang, Jiezhong Cao, Yuchen Fan, Kai Zhang, Rakesh Ranjan, Yawei Li, Radu Timofte, and Luc Van Gool. Vrt: A video restoration transformer. *IEEE Transactions on Image Processing*, 2024. 3
- [36] Bee Lim, Sanghyun Son, Heewon Kim, Seungjun Nah, and Kyoung Mu Lee. Enhanced deep residual networks for single image super-resolution. In *Proceedings of the IEEE conference on computer vision and pattern recognition workshops*, pages 136–144, 2017. 1, 2, 5
- [37] Ce Liu and Deqing Sun. A bayesian approach to adaptive video super resolution. In *The 24th IEEE Conference on Computer Vision and Pattern Recognition, CVPR 2011, Colorado Springs, CO, USA, 20-25 June 2011*, pages 209–216. IEEE Computer Society, 2011. 5
- [38] Ze Liu, Yutong Lin, Yue Cao, Han Hu, Yixuan Wei, Zheng Zhang, Stephen Lin, and Baining Guo. Swin transformer: Hierarchical vision transformer using shifted windows. In *Proceedings of the IEEE/CVF international conference on computer vision*, pages 10012–10022, 2021. 2
- [39] Jun Lyu, Shuo Wang, Yapeng Tian, Jing Zou, Shunjie Dong, Chengyan Wang, Angelica I Aviles-Rivero, and Jing Qin. Stadnet: Spatial-temporal attention-guided dual-path network for cardiac cine mri super-resolution. *Medical Image Analysis*, 94:103142, 2024. 1
- [40] Ben Mildenhall, Pratul P Srinivasan, Matthew Tancik, Jonathan T Barron, Ravi Ramamoorthi, and Ren Ng. Nerf: Representing scenes as neural radiance fields for view synthesis. In *Proceedings of the European Conference on Computer Vision*, pages 405–421, 2020. 1
- [41] Thomas Müller, Alex Evans, Christoph Schied, and Alexander Keller. Instant neural graphics primitives with a multiresolution hash encoding. *ACM Transactions on Graphics*, 41(4):102:1–102:15, 2022. 2, 3
- [42] Seungjun Nah, Tae Hyun Kim, and Kyoung Mu Lee. Deep multi-scale convolutional neural network for dynamic scene deblurring. In *2017 IEEE Conference on Computer Vision and Pattern Recognition, CVPR 2017, Honolulu, HI, USA, July 21-26, 2017*, pages 257–265. IEEE Computer Society, 2017. 5
- [43] Sung Cheol Park, Min Kyu Park, and Moon Gi Kang. Super-resolution image reconstruction: a technical overview. *IEEE Signal Processing Magazine*, 20(3):21–36, 2003. 1
- [44] Mehdi SM Sajjadi, Raviteja Vemulapalli, and Matthew Brown. Frame-recurrent video super-resolution. In *Proceedings of the IEEE conference on computer vision and pattern recognition*, pages 6626–6634, 2018. 3
- [45] Shuwei Shi, Jinjin Gu, Liangbin Xie, Xintao Wang, Yujiu Yang, and Chao Dong. Rethinking alignment in video super-resolution transformers. *Advances in Neural Information Processing Systems*, 35:36081–36093, 2022. 1
- [46] Xingjian Shi, Zhourong Chen, Hao Wang, Dit-Yan Yeung, Wai-Kin Wong, and Wang-chun Woo. Convolutional lstm network: A machine learning approach for precipitation

- nowcasting. *Advances in neural information processing systems*, 28, 2015. 3
- [47] Vincent Sitzmann, Julien N.P. Martel, Alexander W. Bergman, David B. Lindell, and Gordon Wetzstein. Implicit neural representations with periodic activation functions. In *Advances in Neural Information Processing Systems*, pages 7462–7473, 2020. 1, 3
- [48] Jaejun Soh, Gwanghyun Park, Sunghyun Cho, Jeonghyeon Shin, and Bohyung Han. Piifgan: Periodic implicit image function for general image super-resolution. In *Proceedings of the IEEE/CVF Conference on Computer Vision and Pattern Recognition*, pages 18917–18926, 2022. 3
- [49] Chao Sun, Yifan Chen, Hao Xu, and Andreas Geiger. Directvoxgo: Fast direct voxel grid optimization for radiance fields reconstruction. *Proceedings of the IEEE/CVF Conference on Computer Vision and Pattern Recognition*, pages 5459–5469, 2022. 3
- [50] Matthew Tancik, Pratul P. Srinivasan, Ben Mildenhall, Sara Fridovich-Keil, Neel Raghavan, Utkarsh Singhal, Ravi Ramamoorthi, Jonathan T. Barron, and Ren Ng. Fourier features let networks learn high frequency functions in low dimensional domains. In *Advances in Neural Information Processing Systems*, pages 7537–7547, 2020. 1, 3
- [51] Xin Tao, Hongyun Gao, Renjie Liao, Jue Wang, and Jiaya Jia. Detail-revealing deep video super-resolution. In *Proceedings of the IEEE international conference on computer vision*, pages 4472–4480, 2017. 1, 3
- [52] Yapeng Tian, Yulun Zhang, Yun Fu, and Chenliang Xu. Tdan: Temporally-deformable alignment network for video super-resolution. In *Proceedings of the IEEE/CVF conference on computer vision and pattern recognition*, pages 3360–3369, 2020. 1, 3
- [53] Radu Timofte, Eirikur Agustsson, Luc Van Gool, Ming-Hsuan Yang, and Lei Zhang. Ntire 2017 challenge on single image super-resolution: Methods and results. In *Proceedings of the IEEE conference on computer vision and pattern recognition workshops*, pages 114–125, 2017. 5
- [54] Xintao Wang, Kelvin CK Chan, Ke Yu, Chao Dong, and Chen Change Loy. Edvr: Video restoration with enhanced deformable convolutional networks. In *Proceedings of the IEEE/CVF conference on computer vision and pattern recognition workshops*, pages 0–0, 2019. 1, 3
- [55] Rongyuan Wu, Tao Yang, Lingchen Sun, Zhengqiang Zhang, Shuai Li, and Lei Zhang. Seesr: Towards semantics-aware real-world image super-resolution. In *Proceedings of the IEEE/CVF conference on computer vision and pattern recognition*, pages 25456–25467, 2024. 3
- [56] Gang Xu, Jun Xu, Zhen Li, Liang Wang, Xing Sun, and Ming-Ming Cheng. Temporal modulation network for controllable space-time video super-resolution. In *Proceedings of the IEEE/CVF conference on computer vision and pattern recognition*, pages 6388–6397, 2021. 3
- [57] Jiaqi Xu, Xiaowei Hu, Lei Zhu, Qi Dou, Jifeng Dai, Yu Qiao, and Pheng-Ann Heng. Video dehazing via a multi-range temporal alignment network with physical prior. In *Proceedings of the IEEE/CVF Conference on Computer Vision and Pattern Recognition*, pages 18053–18062, 2023. 1
- [58] Tianfan Xue, Baian Chen, Jiajun Wu, Donglai Wei, and William T Freeman. Video enhancement with task-oriented flow. *International Journal of Computer Vision*, 127:1106–1125, 2019. 3
- [59] Xi Yang, Chenhang He, Jianqi Ma, and Lei Zhang. Motion-guided latent diffusion for temporally consistent real-world video super-resolution. In *European Conference on Computer Vision*, pages 224–242. Springer, 2025. 1
- [60] Peng Yi, Zhongyuan Wang, Kui Jiang, Junjun Jiang, and Jiayi Ma. Progressive fusion video super-resolution network via exploiting non-local spatio-temporal correlations. In *Proceedings of the IEEE/CVF international conference on computer vision*, pages 3106–3115, 2019. 3
- [61] Peng Yi, Zhongyuan Wang, Kui Jiang, Junjun Jiang, Tao Lu, Xin Tian, and Jiayi Ma. Omniscient video super-resolution. In *Proceedings of the IEEE/CVF international conference on computer vision*, pages 4429–4438, 2021. 3
- [62] Alex Yu, Sara Fridovich-Keil, Matthew Tancik, Jonathan Ling, Qinhong Liao, Andrew Trevithick, Steven Boyd, Vidya Prabhakaran, Ravi Ramamoorthi, Angjoo Kanazawa, and Jonathan T Barron. Plenoxels: Radiance fields without neural networks. *Proceedings of the IEEE/CVF Conference on Computer Vision and Pattern Recognition*, pages 5501–5510, 2022. 3
- [63] Fanghua Yu, Jinjin Gu, Zheyuan Li, Jinfan Hu, Xiangtao Kong, Xintao Wang, Jingwen He, Yu Qiao, and Chao Dong. Scaling up to excellence: Practicing model scaling for photo-realistic image restoration in the wild. In *Proceedings of the IEEE/CVF Conference on Computer Vision and Pattern Recognition*, pages 25669–25680, 2024. 3
- [64] Roman Zeyde, Michael Elad, and Matan Protter. On single image scale-up using sparse-representations. In *Curves and Surfaces - 7th International Conference, Avignon, France, June 24-30, 2010, Revised Selected Papers*, pages 711–730. Springer, 2010. 5
- [65] Yulun Zhang, Kunpeng Li, Kai Li, Lichen Wang, Bineng Zhong, and Yun Fu. Image super-resolution using very deep residual channel attention networks. In *Proceedings of the European conference on computer vision (ECCV)*, pages 286–301, 2018. 2
- [66] Yulun Zhang, Kunpeng Li, Kai Li, Lichen Wang, Bineng Zhong, and Yun Fu. Image super-resolution using very deep residual channel attention networks. In *Proceedings of the European Conference on Computer Vision*, pages 286–301, 2018. 1
- [67] Shangchen Zhou, Peiqing Yang, Jianyi Wang, Yihang Luo, and Chen Change Loy. Upscale-a-video: Temporal-consistent diffusion model for real-world video super-resolution. In *Proceedings of the IEEE/CVF Conference on Computer Vision and Pattern Recognition*, pages 2535–2545, 2024. 1